Numerical Investigation and Optimization of a Flushwall Injector for Scramjet Applications at Hypervelocity Flow Conditions

Tomasz G. Drozda,* Rajiv R. Shenoy,† Erik L. Axdahl,† and Robert A. Baurle,†
NASA Langley Research Center, Hampton, VA 23681

An investigation utilizing Reynolds-averaged simulations (RAS) was performed in order to demonstrate the use of design and analysis of computer experiments (DACE) methods in Sandia's DAKOTA software package for surrogate modeling and optimization. These methods were applied to a flowpath fueled with an interdigitated flushwall injector suitable for scramjet applications at hypervelocity conditions and ascending along a constant dynamic pressure flight trajectory. The flight Mach number, duct height, spanwise width, and injection angle were the design variables selected to maximize two objective functions: the thrust potential and combustion efficiency. Because the RAS of this case are computationally expensive, surrogate models are used for optimization. To build a surrogate model a RAS database is created. The sequence of the design variables comprising the database were generated using a Latin hypercube sampling (LHS) method. A methodology was also developed to automatically build geometries and generate structured grids for each design point. The ensuing RAS analysis generated the simulation database from which the two objective functions were computed using a one-dimensionalization (1D) of the three-dimensional simulation data. The data were fitted using four surrogate models: an artificial neural network (ANN), a cubic polynomial, a quadratic polynomial, and a Kriging model. Variance-based decomposition showed that both objective functions were primarily driven by changes in the duct height. Multiobjective design optimization was performed for all four surrogate models via a genetic algorithm method. Optimal solutions were obtained at the upper and lower bounds of the flight Mach number range. The Kriging model predicted an optimal solution set that exhibited high values for both objective functions. Additionally, three challenge points were selected to assess the designs on the Pareto fronts. Further sampling among the designs of the Pareto fronts may be required to lower the surrogate model errors and perform more accurate surrogate-model-based optimization.

I. Introduction

THE design of fuel injector systems, fuel-air mixing, and efficient combustion and flameholding are key fluid dynamic challenges for optimal designs of scramjet flowpaths. Attempts to enhance the fuel-air mixing, while reducing total pressure losses, thereby improving thrust potential, have received a great deal of attention over the years.[1] Although a certain amount of total pressure loss is expected due to the desired effect of molecular mixing of the fuel and air, further losses will reduce the thrust potential of the engine and should, therefore, be minimized.

The Enhanced Injection and Mixing Project (EIMP) being conducted at the NASA Langley Research Center, represents an effort to achieve more rapid mixing at high flow speeds.[2] The EIMP aims to investigate scramjet fuel injection and mixing physics, improve the understanding of underlying physical processes, and develop enhancement strategies relevant to flight Mach numbers greater than 8. Since a shorter combustor results in a lighter vehicle, the ultimate goal is to minimize the overall combustor length, while producing sufficient thrust at minimal losses. Furthermore, it is beneficial to obtain functional relationships between the relevant performance metrics, such as combustion efficiency and thrust potential, and the flowpath geometrical parameters, such as spanwise injector spacing and duct height in order to guide designs. The effect of varying the flight conditions, such as the Mach number,[3] can also be included. The goal of the present study is to demonstrate the use of the design and analysis of computer experiments (DACE)

*Research Aerospace Engineer, Hypersonic Airbreathing Propulsion Branch, AIAA Associate Fellow.
†Research Engineer, Analytical Mechanics Associates, Inc., AIAA Member.

methods available in DAKOTA[4] (an object-oriented framework for design optimization, parameter estimation, uncertainty quantification, and sensitivity analysis) for optimization of an interdigitated flushwall injector in a straight duct. Because the Reynolds-averaged simulations (RAS) used are computationally expensive and therefore inefficient for direct optimization, surrogate models are developed and used with a genetic algorithm to drive optimization in order to make optimization computationally affordable.

II. Injector Geometry and Flow Conditions

The flushwall injector used in the current work introduces a number of flow features around the injection site that interact to produce a fluidic blockage. A bow shock forms upstream of the injection plume creating total pressure losses and aerodynamic blockage by forcing the air to flow around the fuel plume. The fuel plume entering the high-speed crossflow generates a counterrotating vortex pair, which becomes the main mechanism for stirring the fuel into the air. However, unlike a fuel placement device, such as a strut, the extent to which the fuel penetrates into the airflow is governed by fluidic considerations.[1,5–7] The jet penetration has been shown to be primarily proportional to the ratio of the orthogonal components of the dynamic pressure (or momentum flux) of the main air and the fuel jet, and is further enhanced by matching the static pressure at the exit of the fuel injector to the static pressure of the air just upstream of the fuel plume and downstream of the bow shock.

Top-down and side views and dimensional details of the flushwall injector geometry are shown in Fig.1. The port's exit interface shape is derived from the multiobjective optimization work of Ogawa.[8] The injector port has a rectangular cross section with the longer dimension aligned with the streamwise direction. Ogawa and Boyce[9] showed that a high aspect ratio rectangular cross-section port was desirable for high mixing efficiency and fuel penetration. More recently, Ogawa[8] showed that a high aspect ratio oval injector cross-section offers a slight improvement in mixing efficiency over a similar aspect ratio rectangular injector. The injection angle α, i.e., the angle of the port with respect to the streamwise direction, is variable and the port rotates about an axis coinciding with the intersection of the upstream port wall and the combustor plate as detailed in Fig.1. The injector also contains an expansion section with a 6 degree half-angle. The port's width is fixed at 0.1392 inches and the port's throat height is 0.1541 inches. The expansion area ratio is approximately 2.95 at the exit height of 0.4551 inches. The area of the injector at the fuel

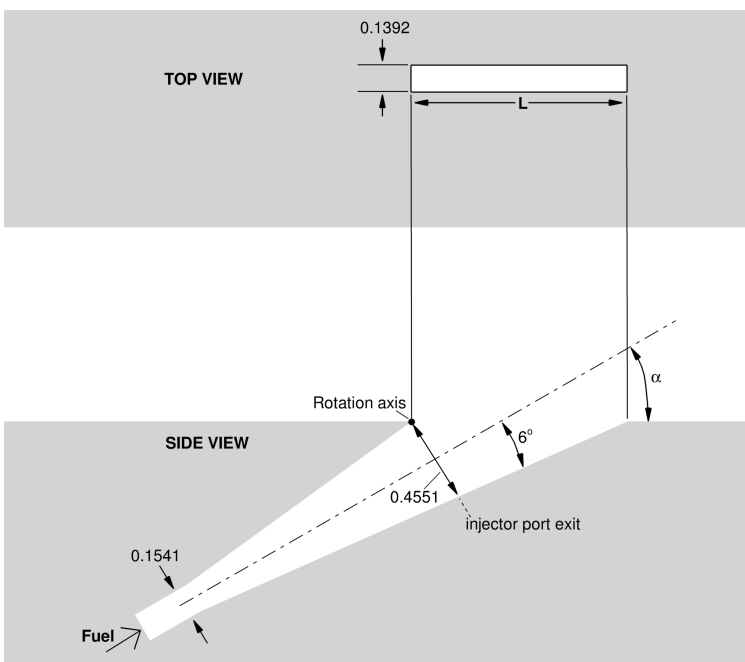

Figure 1. Dimensional details of the baseline flushwall injector (dimensions are in inches). The injection angle is denoted by α. The injector port intersects the combustor wall across an interface with length L.

exit plane varies with the injection angle. This area has length L of about 1.11 and 0.4551 inches at $\alpha = 30°, 90°$, respectively.

Figure 2 shows a schematic view of the flow cross section with its interdigitated arrangement of the flushwall injectors. An infinite row of interdigitated injectors is simulated. The duct height h is defined as the distance between the upper and lower combustor walls, while the spanwise spacing w is defined as the distance between two adjacent injector ports. The intended fueling area (IFA), denoted by dashed lines, is defined as the portion of the cross-sectional area of the duct that each injector is expected to fuel independently of the others. For the flushwall injector, an appropriate choice for the IFA is the half-height times the spanwise spacing ($h/2 \times w$).

The flight trajectory of interest in this study takes the vehicle across a range of Mach numbers from 8 to 15 along a constant dynamic pressure trajectory of 1500 psf. To obtain the flow conditions at the flowpath entrance, the freestream air is compressed to 50.66 kPa with an inlet model assuming 95% isentropic efficiency and 99% adiabatic efficiency. The kinetic energy efficiency of this notional inlet is about 98%. The total inlet contraction ratio ranges from about 7.3 at a flight Mach number of 8 to about 20.0 at a flight Mach number of 15. Because the flowpath inflow area, defined by the product of the duct height and spanwise injector separation width, varies independently of the flight Mach number, the notional vehicle inlet capture area changes as a function of the flight Mach number. The combustor inflow Mach number ranges from about 3.7 to 6.4 as the flight Mach number increases. The freestream conditions for flight Mach numbers of 8 and 15 are shown in Table 1. A thermally perfect mixture of 21% oxygen (O_2) and 79% nitrogen (N_2) by volume was used for the air in the simulations. Hydrogen fuel is supplied at a total temperature of approximately 1200 K and its mass flow rate for each injector was computed based on an equivalence ratio (ER) of 0.75 over the IFA.

Table 1. Freestream conditions for the extrema of flight Mach numbers in the current simulations.

Alt. (km)	Mach No.	Q (kPa)	p (kPa)	T (K)	T_0† (K)	p_0† (MPa)
28.0	8.0	71.82	1.6048	232.4	2753.9	24.78
36.6	15.0	71.82	0.4565	249.4	8816.6	1333.2

†Value based on frozen composition of air

III. Computational Methodology

The numerical simulations were performed using the Viscous Upwind aLgorithm for Complex flow ANalysis (VULCAN-CFD) code.[10] VULCAN-CFD is a cell-centered, finite-volume solver widely used for high-speed flow simulations. For this work, Reynolds-averaged simulations (RAS) were performed using structured, multi-block grids. The advective terms were computed using the Monotone Upstream-Centered Scheme for Conservation Laws (MUSCL) scheme[11] with the Low-Dissipation Flux-Split Scheme (LDFSS) of Edwards.[12] The thermodynamic

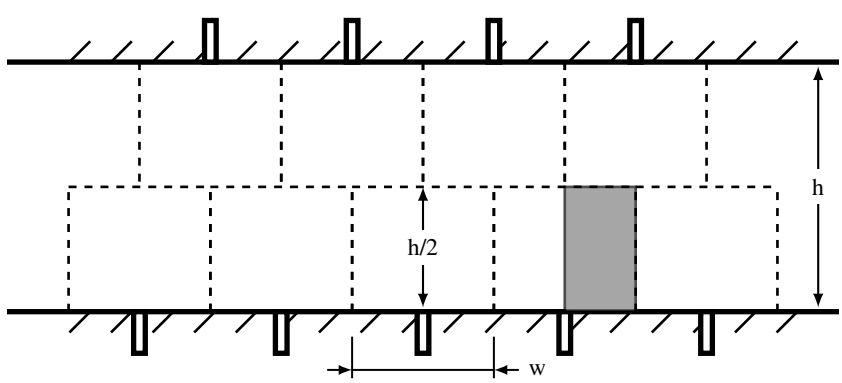

Figure 2. Schematic of the cross-section view of the ducted flowpath with a row of interdigitated flushwall injectors The region between dashed lines denote the IFA for each injector and the shaded area illustrates the cross-section of the computational domain used.

properties of the mixture components were computed using the curve fits of McBride et al.[13] The governing equations were integrated using an implicit diagonalized approximate factorization (DAF) method.[14] The current work used the Menter Baseline two-equation turbulence model.[15] The Reynolds heat and species mass fluxes were modeled using a gradient diffusion model with turbulent Prandtl and Schmidt numbers of 0.9 and 0.5, respectively. The chemical reactions are modeled using the nine-species / nineteen-reaction hydrogen air kinetic model of Conaire et al.,[16] neglecting turbulence-chemistry interactions. Wilcox wall matching functions[17] were also used, however, their implementation in VULCAN-CFD includes a modification that allows the simulations to recover the integrate-to-the-wall behavior as the value of normalized wall-distance, y^+, approaches one. All simulations were converged until the total integrated mass flow rate and the total integrated heat flux on the walls remained constant to at least 4 decimal points. This typically occurred when the value of the L_2-norm of the steady-state equation-set residual decreased by about 3–4 orders of magnitude. To conserve the available computational resources, all the simulations were split into elliptic and space-marching regions. The elliptic region contained the inflow of the domain, the injector bodies, and up to 6.5 inches downstream of the injection plane. The computational cell count was about equal in both regions, but the computational cost associated with solving the space-marching region was about an order of magnitude lower than that for the elliptic region. Past simulation experience[3] with similar injector configurations have shown that this approach accurately simulates the flow as compared to using a single, fully elliptic region.

The computational domain is illustrated in Fig. 3. The inflow and outflow planes are placed at 9 inches upstream and 25 inches downstream, respectively, of the fuel injection plane located at X = 0. The left symmetry plane bisects the port and the right symmetry plane is located halfway between adjacent injector ports at a distance of $w/2$ from the left symmetry plane. The interdigitated symmetry is also leveraged by utilizing a pair of polar periodic boundary conditions on the top plane of the computational domain. The cross-sectional area of the computational domain corresponds to half the IFA and is shaded in gray in Fig. 2.

IV. Objective Functions, Design Variables, Grid Generation, and Surrogate Models

The performance of the fuel injection was evaluated using two metrics of interest. The first metric of interest is the thrust potential. This metric is obtained by expanding one-dimensional[18] values obtained from the simulations at each streamwise location through an ideal (isentropic) thrust nozzle. In the current work, this expansion process is evaluated until the flow reaches the static pressure at the combustor flowpath entrance. Another possibility would be to expand the flow to the freestream static pressure. The choice to expand the flow to the flowpath entrance static pressure is to limit the thrust potential values to those corresponding to the flowpath component only rather than the entire vehicle. The thrust potential is computed from:

$$TP = \dot{m}_e u_e + p_e A_e - \dot{m}_i u_i - p_i A_i \tag{1}$$

where TP is the stream thrust potential (not net thrust potential); $\dot{m}$, u, p, and A, are the mass flow rate, velocity, static pressure, and the area, respectively, with subscripts e and i denoting conditions at the thrust nozzle exit plane, and the flowpath entrance (inflow). Since the mass flow rate through the flowpath varies with the flight condition and the IFA, it is beneficial to normalize the thrust potential by the inflow mass flow rate to enable useful comparisons as the flight conditions change. The resulting mass-flow specific stream thrust potential is:

$$TP_m \equiv \frac{TP}{\dot{m}_i} = \frac{\dot{m}_e u_e + p_e A_e - p_i A_i}{\dot{m}_i} - u_i. \tag{2}$$

This metric represents an ideal potential mass-flow specific stream thrust that could be obtained when a flowpath of interest is truncated at a given streamwise location and coupled at that location to an ideal thrust nozzle. However, the flow in the thrust nozzle is assumed to be chemically "frozen" starting at the point of expansion, and therefore, this metric does not account for any additional mixing (thrust loss) and reaction (thrust gain) during the expansion process. For the rest of this paper, this mass-flow specific stream thrust potential will be referred to as the thrust potential for brevity (TP_m). All of the total pressure losses still appear as a decrease in the value of the thrust potential, however, the pressure losses due to chemical reactions, which energize the flow, could increase the value of the thrust potential.

The second metric of interest is the combustion efficiency, which quantifies how completely a given flowpath is able to process a mixture of fuel and air into combustion products, thereby enabling heat release into the flow. The combustion efficiency is selected in this work in addition to the thrust potential in order to incorporate designs that

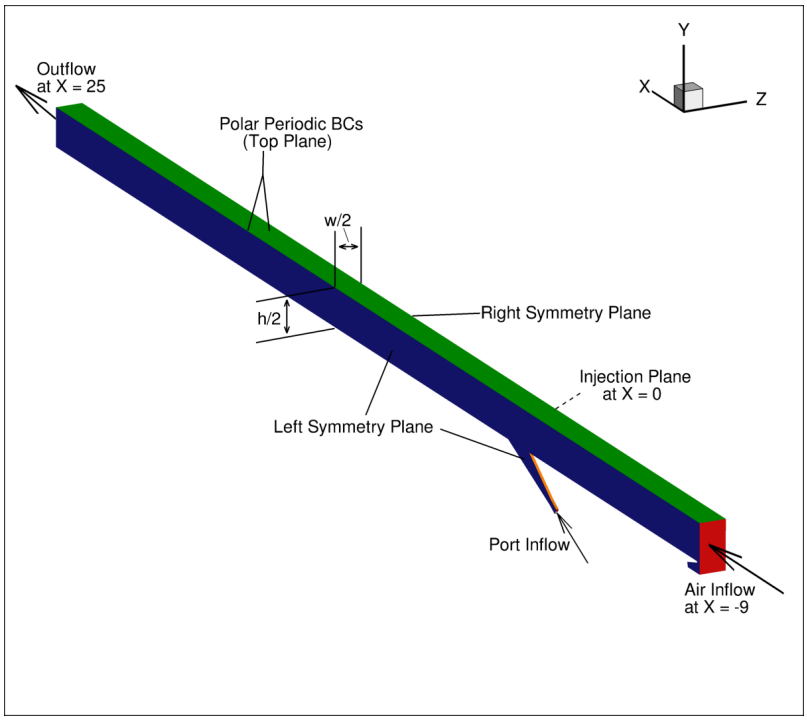

(a) View showing entire combustor with relevant boundary conditions and streamwise stations.

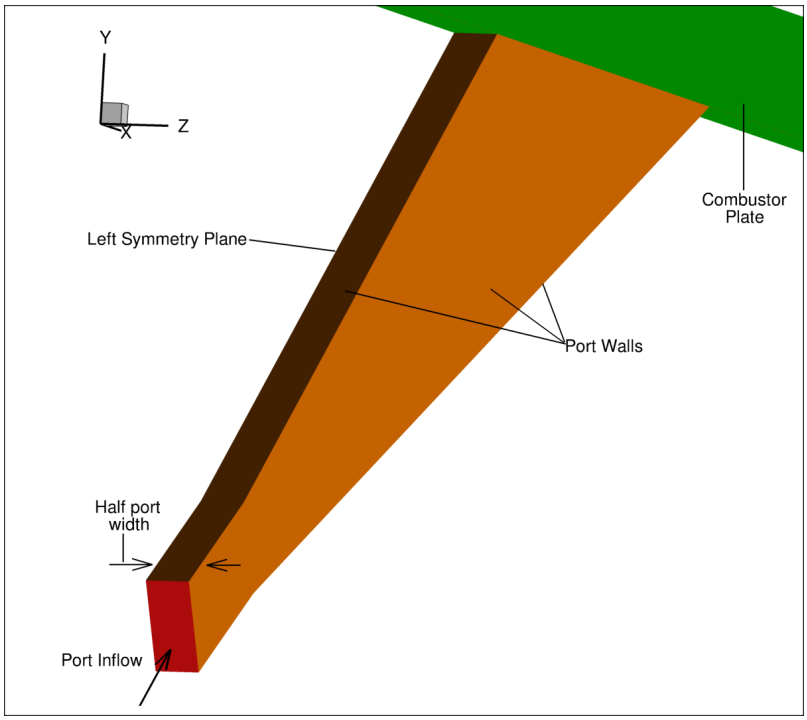

(b) Detailed view of injector port and combustor plates.

Figure 3. Computational domain of the combustor with relevant details. All dimensions are in inches.

promote fuel mixing (and, thereby, combustion) as desirable, rather than designs that simply augment thrust via low-angle fuel injection. In this work, because the equivalence ratio is less than one, the combustion efficiency is computed based on the depleted fuel mass flow rate, i.e.,

$$\eta_c = 1 - \frac{\dot{m}_f}{\dot{m}_{f,tot}} \tag{3}$$

where $\dot{m}_f$ and $\dot{m}_{f,tot}$ are the integrated mass flow rates of fuel at a streamwise location of interest and the total injected fuel flow rate, respectively.

Four parameters are used as design variables. These are the flight Mach number M, duct height h, spanwise spacing w, and the injection angle α. The bounds of these variables were chosen based on research interests and subject matter expertise guided by previous work. The optimization problem can be characterized as follows: Both

maximize:	thrust potential: $TP_m(m/s)$
	combustion efficiency: η_c
subject to:	flight Mach number: $8.0 \leq M \leq 15.0$
	duct height: $1.0 \leq h(in) \leq 3.0$
	spanwise spacing: $0.8 \leq w(in) \leq 2.0$
	injection angle: $30° \leq \alpha \leq 90°$

optimization quantities are obtained at the exit of the domain, i.e., 25 inches downstream of the fuel injection plane. The flight Mach number bounds reflect the flight conditions of interest from previous work,[3] while the duct height and spanwise spacing bounds are selected based on estimates of where optimal solutions are expected. The injection angle bounds were selected based on the optimization effort of Ogawa.[8]

Simulation grids were generated using the GoHypersonic Inc. LINK3D software,[19] which enables efficient, parallel structured grid generation that is amenable to geometric modifications and design optimization. A methodology was developed that automatically generates the required geometry and performs grid smoothing and clustering based on the geometrical design parameters. First, using the geometric design variables, i.e., the duct height, spanwise spacing, and injection angle, geometry curves and surfaces are generated. Because the structured grid topology nodes reside in one-dimensional and two-dimensional coordinates with respect to their associated geometry curves and surfaces, respectively, the nodal locations can be automatically updated in response to a geometric modification. This allows for the same grid topology to be reused for any geometry in the design space. The second step involved assigning dimensions for a small group of edge families in the topology so that a nominal spacing of 0.01 inches was achieved. A computational grid dependence study was previously conducted by Drozda et al.[20] showing that this nominal spacing allows for numerical errors of approximately 5% in total pressure recovery and mixing efficiency. Finally, the structured grids, which ranged between 4.8 million cells to 23.8 million cells, were smoothed and clustered using LINK3D's parallel grid engine on a desktop machine, typically in one hour. Figure 4 shows slices of the grid at the left symmetry plane for two different geometric configurations. While the first case has a small injection angle and a large duct height, the second has a large injection angle and a smaller height.

Because RAS is computationally expensive, a surrogate model is constructed to provide rapid predictions for the thrust potential and combustion efficiency as a function of the four parameters. Several surrogate models are evaluated. These are based on quadratic and cubic polynomials, Kriging, and artificial neural networks (ANNs). To obtain the surrogate model, a RAS database is first created by performing 66 RAS solutions for various combinations of the four parameters: Mach number, duct height, spanwise spacing, and injection angle. The specific values of the four parameters are obtained by using design-of-experiments (DoE). In the current work, Latin hypercube sampling (LHS),[21] augmented by the corner points of the design space (full factorial design for four two-level factors), are used to efficiently fill the multidimensional design space. The total number of RAS simulations is determined from the recommendations in the DAKOTA Theory Manual[21] for a cubic polynomial surrogate model. For four design variables, the minimum number of data samples to form a fully determined linear system and to solve for polynomial coefficients is 35. This number is further increased to 50 to improve the accuracy of cross-validation for the cubic surrogate model, and improve training for the ANN surrogate model. These 50 data points are generated using LHS. Furthermore, an additional 16 points representing corner points of the design space were added to improve surrogate modeling near the boundaries of the design space.

V. Results and Discussion

Scatter plots of the design variables and objective functions for all 66 RAS solutions are shown in Fig. 5. The markers are colored by the value of the thrust potential. The small and large marker sizes denote the LHS points and design space corners, respectively. The first three rows of the plot visually illustrate the space filling characteristics of the LHS. The four design variables appear to reasonably well fill the design space when projected onto any two design variables. The last two rows show the scatter plots of the mixing efficiency and thrust potential vs. each design variable one-at-a-time. The final scatter plot in the lower right corner shows the thrust potential vs. combustion efficiency for all data. Certain trends begin to emerge upon examination of this data:

(a) the highest combustion efficiency occurs at the lowest Mach number, lowest duct height, highest injection angle, and lowest spanwise spacing (although there are cases with high combustion efficiency at both the low injection angle and large spanwise spacing also),

(b) there is an overall negative correlation between the combustion efficiency and duct height,

(c) there is an overall positive correlation between the combustion efficiency and the injection angle,

(d) the highest thrust potential occurs at the highest Mach number, highest duct height, lowest injection angle and highest spanwise spacing (although the second highest thrust potential occurs at the lowest spanwise spacing),

(e) there exists a negative correlation between thrust potential and Mach number,

(f) there exists a positive correlation between thrust potential and duct height,

(g) high combustion efficiency for Mach numbers greater than about 12 and duct heights less than 1.5 inches result in an overall drag (negative thrust potential) for this flowpath,

(h) there exists a negative correlation between thrust potential and combustion efficiency.

The last row of the scatter plots indicates that desirable values of the thrust potential can be found for this flowpath across the range of Mach numbers of interest provided the flowpath can change geometry in flight. However, high combustion efficiency producing desirable thrust values can only be observed at the lower values of the flight Mach numbers. Therefore, it can be concluded that the desirable thrust potential across the full range of Mach numbers is a result of decreasing fuel injection angle, which aligns the injected fuel stream with the air stream thereby increasing its streamwise momentum. Conversely, increasing the injection angle directs the fuel stream normal to the air stream and,

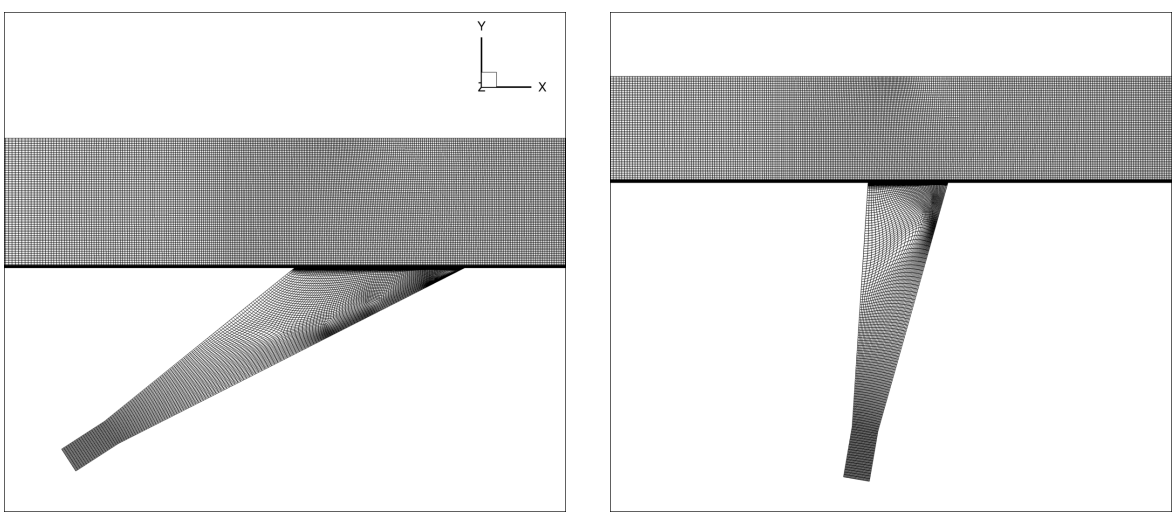

(a) Case with $h = 1.5266$ and $\alpha = 32.892°$.

(b) Case with $h = 1.2497$ and $\alpha = 80.261°$.

Figure 4. Grid slices at the left symmetry plane for two geometric configurations.

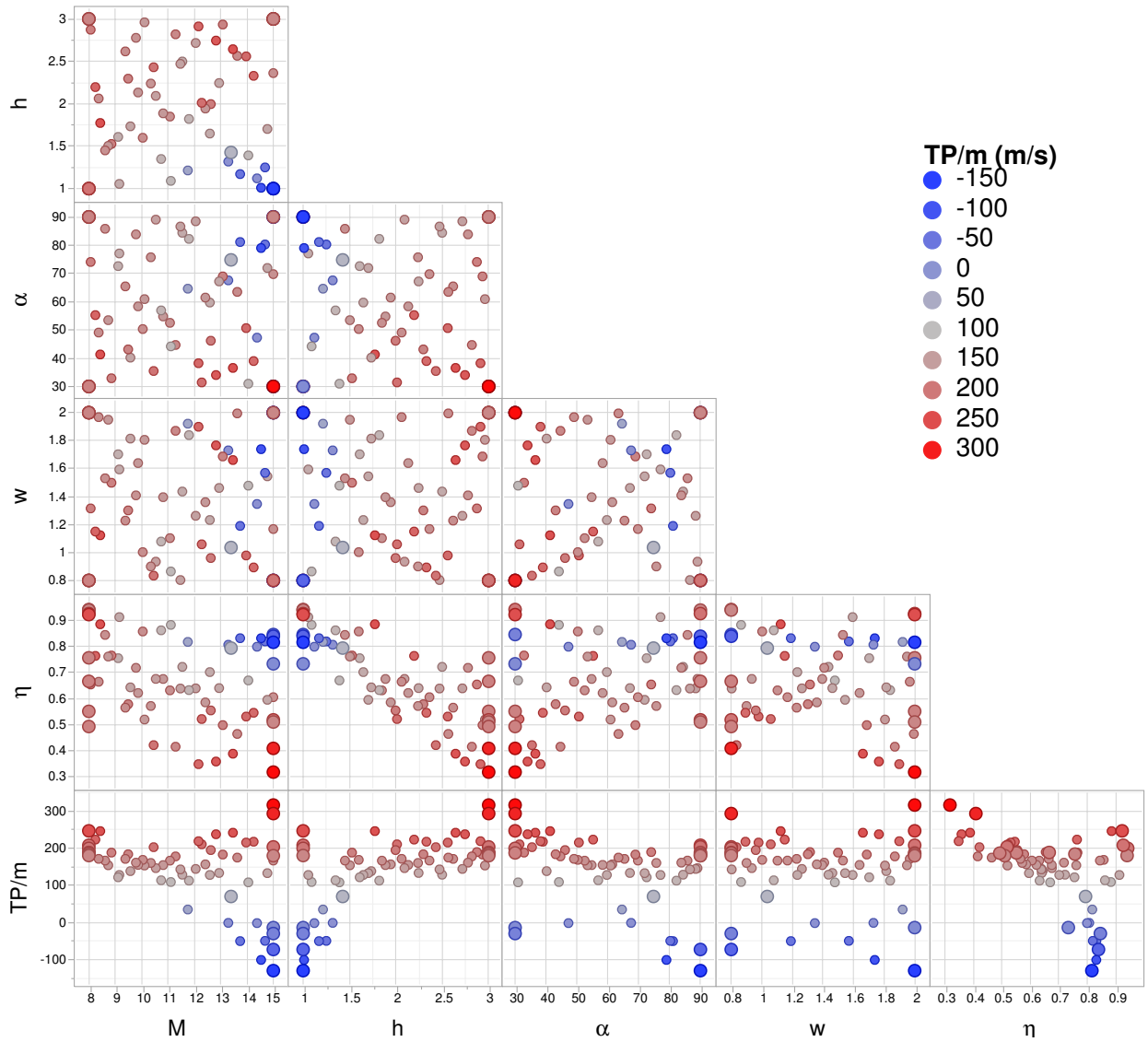

Figure 5. Scatter plots of the design variables and objective functions for all 66 RAS solutions. The markers are colored by the value of the thrust potential. Small and large markers denote the LHS points and design space corners, respectively.

although this promotes more mixing (and thereby combustion) by increasing fuel penetration and blockage, it also increases total pressure losses due to stronger shocks and decreases the axial momentum augmentation. The overall result, at least for the current flowpath, is a tendency for the thrust potential to decrease at higher injection angles, especially for higher Mach numbers, because any thrust gains from heat release due to greater combustion efficiency are offset by the greater losses and reduction in the thrust augmentation from fuel injection. These competing effects are a function of the flight Mach number. Varying the spanwise spacing produced multiple maxima for the thrust potential and desirable values of combustion efficiency over the entire spanwise spacing range, when the duct height is small. The spanwise spacing appears to be less influential when compared against the other design variables.

Four different surrogate models are applied to fit the data using DAKOTA's[4] surrogate model capabilities. These are the quadratic and cubic polynomial models, the Kriging or Gaussian process model with a reduced quadratic trend option, and the artificial neural network (ANN) model. The models are fitted to approximate both objective functions by minimizing the root-mean-squared errors. The overall quality of the fit can be evaluated by computing the fit residuals and 10-fold cross-validation (CV). The results are shown in Table 2. The residual method produces the

deviation of the RAS data from the model's predictions using the full set of training data (i.e., all RAS data points). CV is a technique used to estimate how well a given surrogate model performs when tested against data unused in the surrogate model construction. In the 10-fold CV technique, the simulation data is divided into 10 partitions, and the surrogate model is computed using 9 of the partitions, with the 10th partition set aside for model cross-validation. The process is repeated 10 times, each time setting aside a different partition for validation, resulting in 10 different surrogate models. The root-mean-squared errors for these 10 models with respect to their validation partition are averaged to compute the CV error metric. The residual errors are similar between the ANN and quadratic polynomial models and are lower for the cubic polynomial model. The Kriging model, by definition, will have zero residual error because it passes through all RAS training data. However, 10-fold CV can still be evaluated. Using the 10-fold CV method, the ANN and cubic polynomial models perform the worst, while the Kriging model exhibits the least error.

DAKOTA[4] also enables sensitivity assessment using variance-based decomposition, which is a global sensitivity analysis method that gives a measure of how a model's variability can be attributed to variations in individual input design variables. Variance-based decomposition utilizes the first-order sensitivity index S_i and the total-effect index T_i, also known as Sobol indices. The fraction of the variability in the output, Y, that can be attributed solely to an individual input variable, x_i, is described by the first-order sensitivity index, while the total-effect index describes the fraction of the variability in the output that can be attributed to a given input variable as well as its interactions with other variables. For the four different surrogate models, Sobol indices are computed and plotted in Fig. 6. It is noticeable that the duct height has a major influence on both the thrust potential and combustion efficiency. The flight Mach number and injection angle have a secondary influence on both objective functions, while the spanwise spacing has the least significant influence. The models do not show significant deviation from one another except for the quadratic polynomial fit of the thrust potential, where the spanwise spacing appears even less influential than for the other surrogate fits. The total-effect indices for the thrust potential are significantly greater than their first-order counterparts indicating that the design variables have interactional effects that contribute to the thrust potential output. Unlike, the thrust potential, the total-effect indices for the combustion efficiency show smaller interactional effects from the design variables, suggesting that these variables, in comparison, are relatively independent in affecting this output.

Multiobjective design optimization is performed using these four surrogate models using DAKOTA's[4] multiobjective genetic algorithm. The algorithm starts with a randomly generated population over the design space using the surrogate model, instead of computational fluid dynamics (CFD), to obtain objective function responses. The best design points are then allowed to survive over several generations by performing crossover and mutation operations, and assessing the fitness of each member in the population. The algorithm is terminated when a convergence criteria is met. In this effort, an initial population size of 100 is selected and reproduction requires that two parents generate two offspring. The crossover and mutation rates are set to 0.8 and 0.1, respectively.

Figure 7 (a) shows the final populations of nondominated solutions from the four different surrogate models. For the two objective functions, TP_m and η_c, a nondominated solution means that no further improvement of one function was found without a tradeoff from the other function. The set of these nondominated solutions obtained from each model is also known as a Pareto front. The plots also show the RAS data points obtained from the LHS method marked by open circles and the sixteen corner points of the design space marked by plus signs (+). It should be noted that only a subset of the RAS data points is visible because the thrust potential values are limited by the lower bound of the y-axis. In addition, only a handful of RAS data points can be observed "near" the Pareto fronts, suggesting that the range of the design space variables may need to be expanded and/or that LHS designs that favor design-space boundaries should be considered. The Pareto fronts resulting from the different models show discontinuities that are due to the generation of concave sections of the objective function during the genetic algorithm iterations. These concave sections contain solutions that are dominated by other (nondominated) solutions for both objective functions.

Table 2. Root-mean-squared errors for the different surrogate models.

	Residual		10-fold CV	
	TP_m	η_c	TP_m	η_c
ANN	21.9	0.043	46.4	0.071
Cubic	12.8	0.031	43.7	0.102
Kriging	-	-	25.4	0.057
Quadratic	21.0	0.044	32.2	0.059

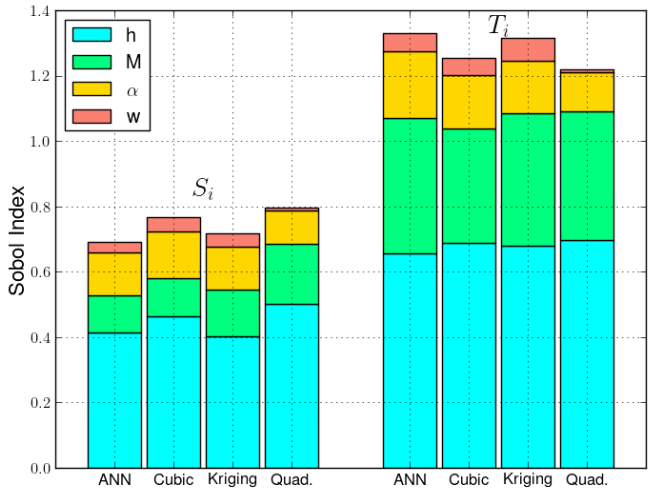

(a) First-order and total-effect indices for TP_m

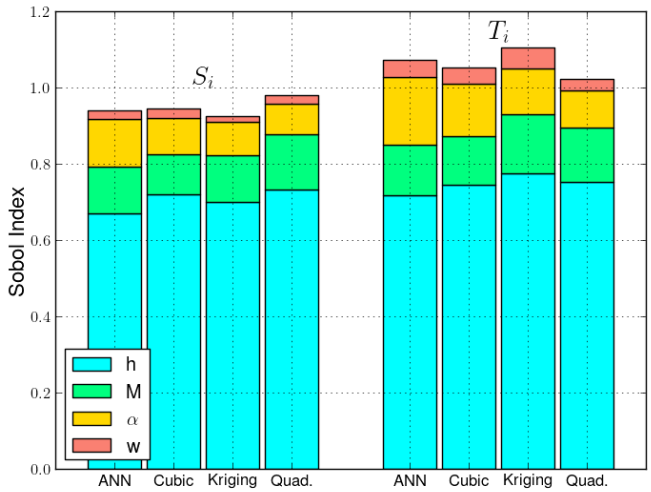

(b) First-order and total-effect indices for η_c

Figure 6. Sensitivity indices computed for the different surrogate models for the effect of design variables on the two objective functions.

The quadratic and cubic polynomial models show optimal designs that produce combustion efficiency greater than one, which is nonphysical. This is because the surrogate models were not constrained by known physical limits. The Pareto fronts resulting from the ANN and quadratic models produce designs that are suboptimal to the two designs from the training data, which have values of thrust potential and combustion efficiency of approximately 245 m/s and 0.90, respectively. Unlike the cubic and Kriging models, the ANN and quadratic models did not fit these training data adequately, resulting in suboptimal Pareto fronts. The ANN, cubic, and quadratic models all show a similar clustering of the Pareto front region where thrust potential is high (between approximately 250 m/s and 310 m/s) and combustion efficiency is low (between approximately 0.4 and 0.5). The Kriging model yields an interesting solution set for the Pareto front, where both the thrust potential and combustion efficiency are high, that is not predicted by the other three models. Such a region is indeed present in the scatter plot of the thrust potential vs. combustion efficiency in Fig. 5, albeit with a lower value of the thrust potential. The variations in the ranges of the Pareto fronts for larger values of the combustion efficiency illustrate that additional RAS sampling to improve surrogate model fidelity and reoptimization might be warranted.

Figure 8 shows the same Pareto fronts and training data with symbols colored by the design variables. The four models show that optimal solutions are bifurcated between the high and low values of the flight Mach number, except

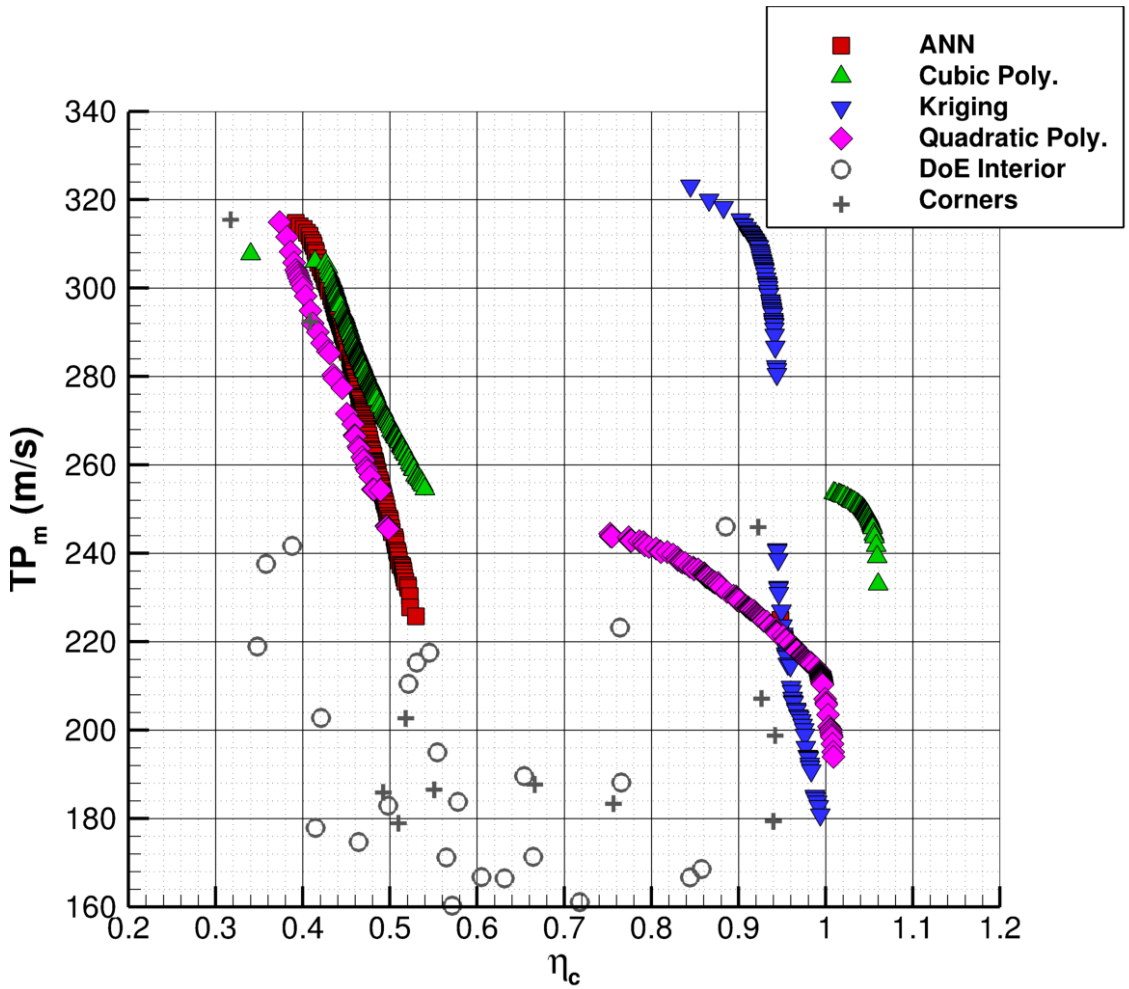

Figure 7. Optimization solutions and training data with the different surrogate models obtained from the final population of the optimization algorithm. Note that the RAS data for which the thrust potential is less than lower limit of the y-axis are not shown.

the ANN model, which shows only a small range of Mach numbers near its highest values. The duct heights for these optimal solution sets are similar for the ANN, cubic, and quadratic models, where low duct height results in optimal solutions that yield high combustion efficiency at the expense of thrust potential (in the lower right region of the plot), and high duct height results in optimal solutions that yield high thrust potential at the expense of combustion efficiency (in the upper left region of the plot). The Kriging solutions show that over the middle range of the duct height, high values of both the thrust potential and combustion efficiency are predicted. The injection angle values vary from low values to midrange values for the optimal solutions resulting from the ANN, cubic, and quadratic models, while the Kriging solutions show the full range of the injection angle values. As expected, the lower the injection angle, the higher the resulting thrust potential, whereas the higher the injection angle, the higher the combustion efficiency and lower the thrust potential due to greater losses. The spanwise spacing values are in the middle range for the optimal solutions resulting from the ANN, cubic, and quadratic model, whereas for the Kriging model, low values of spanwise spacing yields high thrust and high combustion efficiency.

In order to assess the accuracy of the Pareto fronts, three challenge design points that were predicted by the cubic and Kriging models were selected so that RAS may be obtained and compared against the predictions given by the models. These challenge points are provided in Table 3. Only the cubic and Kriging models are challenged because these models predicted the greatest improvement with respect to the training data. The first challenge point selected was a point predicted by the cubic model where thrust potential is high and combustion efficiency is moderate.

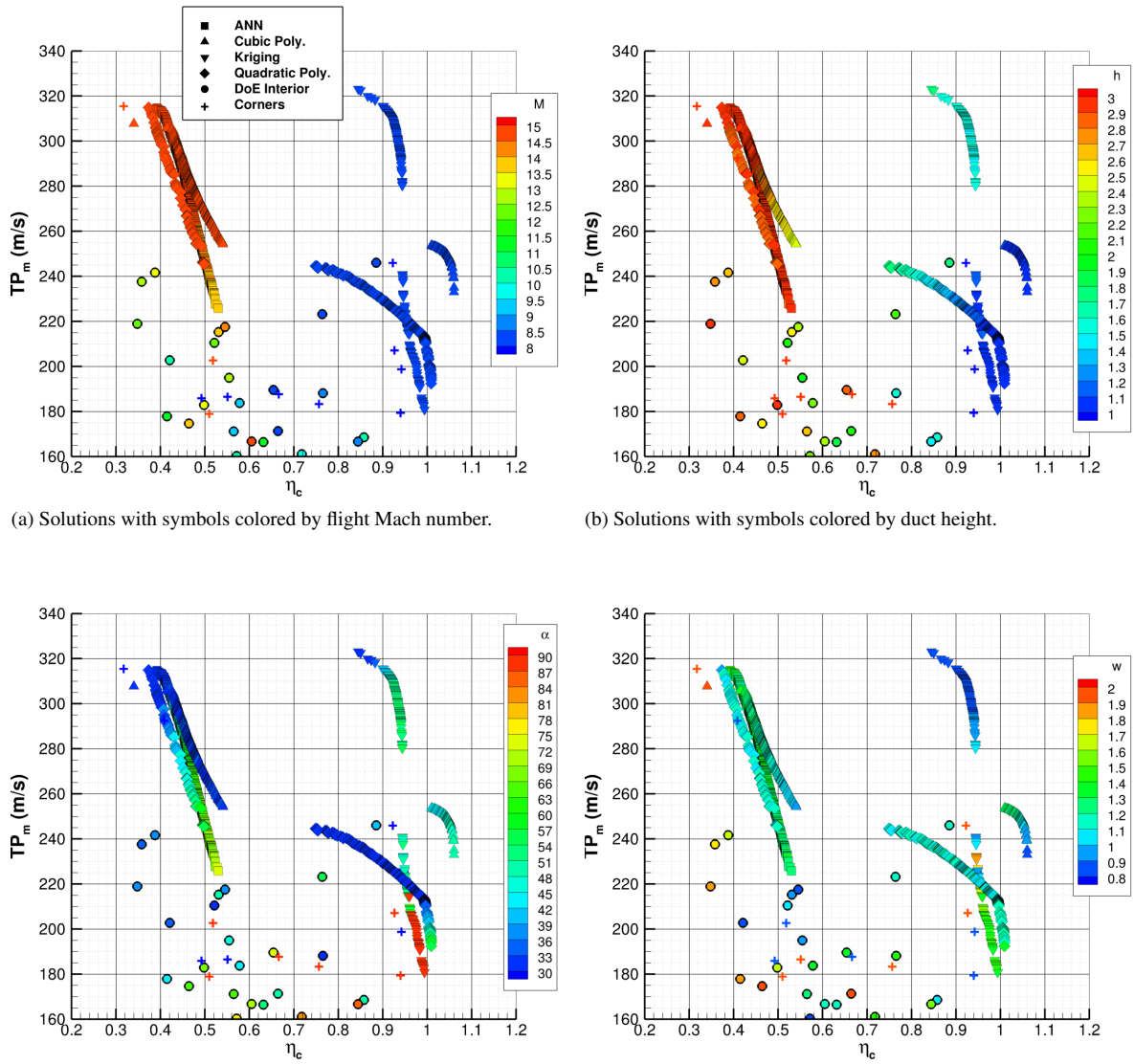

(a) Solutions with symbols colored by flight Mach number.

(b) Solutions with symbols colored by duct height.

(c) Solutions with symbols colored by duct height.

(d) Solutions with symbols colored by duct height.

Figure 8. Optimization solutions and training data with the different surrogate models obtained from the final population of the optimization algorithm and colored by the design variables.

The second challenge point selected was a point predicted by the Kriging model where both the thrust potential and combustion efficiency are high, while the third challenge point selected was a point predicted by the Kriging model where the thrust potential is low but the combustion efficiency is very high.

Flowfields of the three challenge points are shown in the form of Mach contours in Figs. 9 – 11 in order to highlight the varied physics occurring. The black isolines denote the stoichiometric value of the fuel mass fraction. The design of the first challenge point (Fig. 9) is at the upper bound of the flight Mach number and duct height and lower bound of the injection angle. A relatively high thrust potential is obtained by opening up the duct, which reduces the total pressure losses that result from shock reflections, as well as the low injection angle that augments the fuel momentum in the streamwise direction. A low value of mixing efficiency results due to the fuel not penetrating into the air stream and the fuel plume (denoted by the extent of the black isolines) extending up to the combustor exit. The second challenge point (Fig. 10) occurs at the lower bound of the flight Mach number, moderate duct height, and moderate injection angle. The thrust potential is relatively high because the total pressure losses from the shocks are not as high, allowing a small portion of the flow to have a relatively high Mach number up to the combustor exit. The combustion

efficiency is high as the fuel plume mixes well with the air stream and depletes well upstream of the combustor exit. The third challenge point (Fig. 11) occurs at the lower bound of the flight Mach number and duct height, and upper bound of the injection angle. The small duct height, in conjunction with the large injection angle, results in lower thrust potential (high total pressure losses) and greater combustion efficiency as fuel depletes further upstream of the combustor exit than for the second challenge point.

In general, the objective functions obtained for the challenge points are not expected to exactly coincide with those obtained from the surrogate models. To quantify the extent of the mismatch, confidence intervals can be constructed for the surrogate models. Confidence intervals for the Pareto fronts were generated by post-processing all 66 training data points using five sets of 10-fold CV analyses (i.e., repeating the 10-fold CV method 5 times, each time with a different random sorting of the data points into partitions). This method enabled the construction of 50 separate surrogate models for each surrogate model type. Each model, in a set of 50, can be evaluated anywhere in the design space producing an ensemble of 50 possible objective function values. Similar to bootstrapping, this ensemble can then be used to estimate the mean and standard deviation (or minimum and maximum) of the objective functions anywhere in the design space, including the Pareto fronts. One can also obtain 95% confidence intervals that provide an estimate of the error at the Pareto points. It is important to note that these error estimates are obtained by approximating only the training data (i.e., data included in the 9 out of 10 partitions used in the construction of the models) and, thus, will not be as accurate for points sufficiently far away from the training data. Figure 12 shows the Pareto fronts resulting from the cubic and Kriging models with error bars denoting the estimate of the 95% confidence interval. The X marks the RAS result, while the circle highlights the design point on the Pareto front that is being challenged. The first

Table 3. Challenge points listed with model prediction and CFD-generated solution. The model challenged is denoted in parentheses.

	Design Variables				Model		CFD	
Point (Model)	M	h	w	α	TP_m	η_c	TP_m	η_c
1 (Cubic)	14.940	2.9690	1.2771	30.312	304.8	0.4286	271.9	0.4308
2 (Kriging)	8.020	1.5160	0.8044	50.298	309.4	0.9234	270.4	0.8913
3 (Kriging)	8.028	1.0740	1.3933	89.940	200.1	0.9753	199.5	0.9156

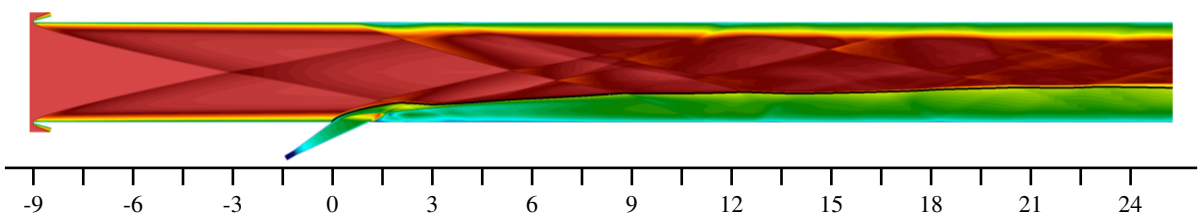

(a) Side view of the port symmetry plane.

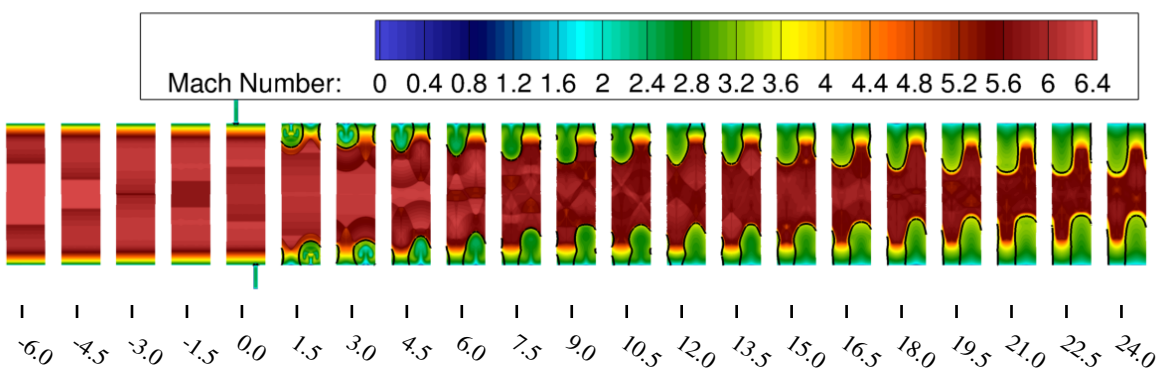

(b) Cross-stream planes.

Figure 9. Mach contours with black isolines denoting stoichiometric value of the fuel mass fraction for challenge point 1.

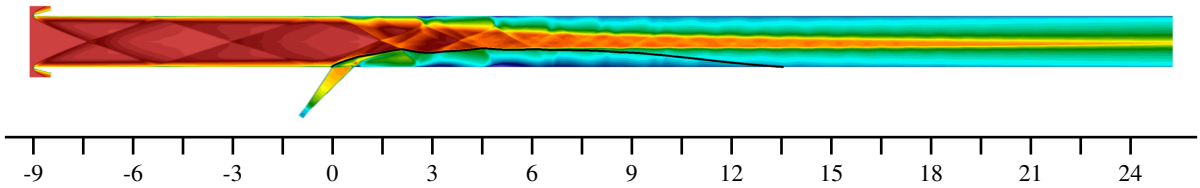

(a) Challenge point 2: Side view of the port symmetry plane.

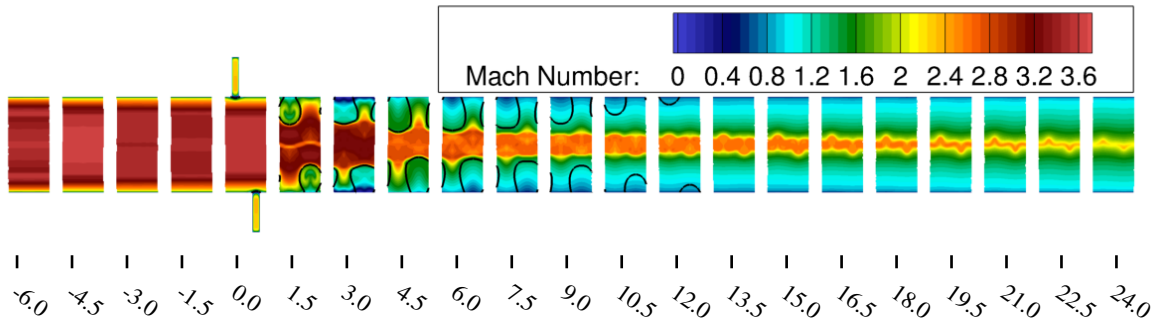

(b) Challenge point 2: Cross-stream planes.

Figure 10. Mach contours with black isolines denoting stoichiometric value of the fuel mass fraction for challenge point 2.

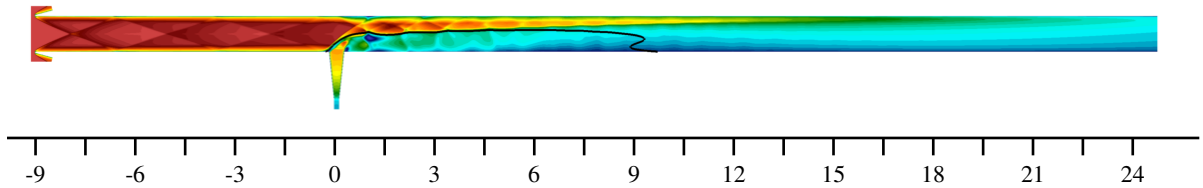

(a) Challenge point 3: Side view of the port symmetry plane.

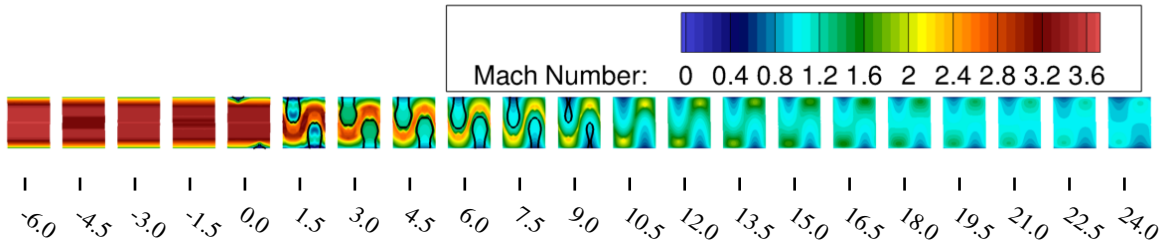

(b) Challenge point 3: Cross-stream planes.

Figure 11. Mach contours with black isolines denoting stoichiometric value of the fuel mass fraction for challenge point 3.

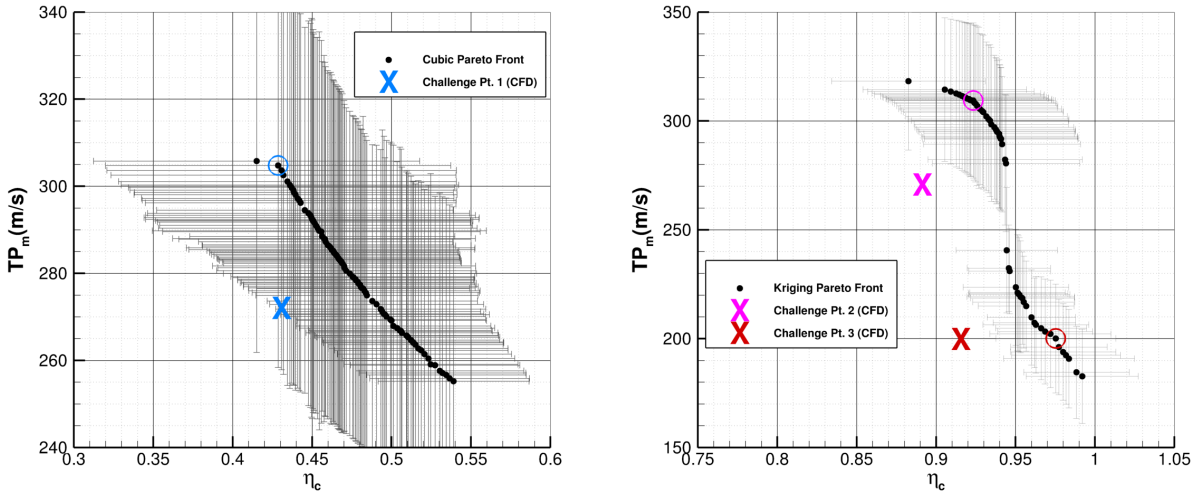

(a) Challenge point 1.

(b) Challenge points 2 and 3.

Figure 12. Comparison of CFD-generated observations at challenge points versus model prediction on Pareto front.

challenge point obtains a good approximation of the CFD-observed value for combustion efficiency, but overpredicts the thrust potential by approximately 32 m/s (nearly 12%). This point falls within its confidence interval estimate. When compared against Fig. 7, this point is close to a corner training data point, where the flight Mach number and duct height are at their maximum values and spanwise spacing and injection angle are at their minimum values. The second challenge point falls within the error estimate bounds of combustion efficiency, but is slightly outside of the error bounds of thrust potential. However, it is interesting to note that this point generated high values for both the thrust potential and the combustion efficiency that show improvement in both thrust potential and combustion efficiency with respect to the original training data that none of the other models predicted. The third challenge point closely approximates the CFD-observed value for the thrust potential but overpredicts the combustion efficiency by nearly 6% and falls outside of its error bounds.

Given the large error estimates for the surrogate models, it may not be possible to perform surrogate-based optimization that can accurately deliver optimal designs. In order to drive the surrogate model errors lower, a set of design points predicted by the first iteration of the optimization could be used to augment the original RAS data set in order to regenerate the surrogate model and perform a second optimization iteration. This process may need to be repeated until the surrogate models are sufficiently converged and the optimization yields sufficiently accurate representation of the Pareto front. However, this iterative process may also prove computationally expensive and without ability to *a priori* predict how many cycles would be required to reach the desired accuracy. Furthermore, it should be noted that, given the current large design space, it may also be impossible to further reduce the surrogate modeling errors. This is because surrogate modeling effectively amounts to an attempt to represent an ensemble of nonlinear steady-state solutions of the partial differential equations (i.e., RAS solutions) by a nonlinear but relatively simple, by comparison, algebraic model. In those cases where surrogate model errors are too large, the extent of the design space may need to be reduced.

In the current problem, optimization was performed over the flight envelope resulting in Pareto fronts that identify optimal combinations of the thrust potential and combustion efficiency over that flight envelope. This is different from performing optimization at fixed values of flight Mach number in order to optimize the geometry for thrust and/or combustion efficiency at that Mach number. Yet another optimization strategy could be to optimize a fixed geometry across the flight Mach number range. In this case, for every combination of geometry design variables, the average values over the flight Mach number range of the thrust potential and combustion efficiency could be optimized. Future efforts will explore such optimization strategies.

VI. Summary and Conclusions

A numerical investigation was conducted in order to demonstrate the use of DACE methods in DAKOTA for surrogate modeling and optimization. These methods were applied to a scramjet flowpath fueled with an interdigitated flushwall injector and ascending along a constant dynamic pressure flight trajectory. The flight Mach number, duct height, spanwise spacing, and injection angle were the design variables for optimizing thrust potential and the combustion efficiency of the flowpath. Because the RAS solutions of this case are computationally expensive, surrogate models were used. To build a surrogate model, a RAS database was created. The sequence of the design variables comprising the database were generated using LHS augmented with the corners of the design space. Using a newly developed automated geometry and structured grid generation methodology, computational grids were efficiently created. The objective functions, thrust potential and combustion efficiency, for the design variables in the RAS database were obtained by performing one-dimensionalization of the three-dimensional simulation data. Four surrogate models, quadratic and cubic polynomials, Kriging, and ANN, were evaluated with respect to their fit and error characteristics. Errors obtained from cross-validation showed that the Kriging model exhibited the least error, while the ANN and the cubic models had the greatest errors. Variance-based decomposition was performed to obtain sensitivity indices. This analysis showed that duct height is the primary driver of both the thrust potential and combustion efficiency. Additionally, the design variables have interactional effects that contribute to the thrust potential response. Multiobjective design optimization was performed using the surrogate models via a multiobjective genetic algorithm. The models showed that optimal solutions exist at both the upper and lower flight Mach number limits. The Kriging model resulted in a Pareto front that yielded high values for both the thrust potential and combustion efficiency that was not captured by the other models. Three challenge points were selected to challenge the optimal solutions predicted by the cubic and Kriging models. Overall the surrogate modeling approach exhibited relatively large uncertainty due to the simplicity of the models used, limited RAS database size, and relatively large extent of the design space. Further sampling among the designs predicted by the Pareto fronts of the surrogate models are warranted in order to improve modeling and perform more accurate surrogate model based optimization.

VII. Acknowledgments

This work is supported by the Hypersonic Technology Project in the Advanced Air Vehicles Program of the NASA Aeronautics Research Mission Directorate (ARMD). Computational resources are provided by the NASA Langley Research Center and the NASA Advanced Supercomputing (NAS) Division.

References

[1] Lee, J., Lin, K.C., and Eklund, D., "Challenges in Fuel Injection for High-Speed Propulsion Systems," *AIAA J.*, Vol. 53, No. 6, 2015, pp. 1405–1423.

[2] Cabell, K., Drozda, T.G., Axdahl, E.L., and Danehy, P.M., "The Enhanced Injection and Mixing Project at NASA Langley," in *JANNAF 46th CS / 34th APS / 34th EPSS / 28th PSHS Joint Subcommittee Meeting*, NTRS Report Number NF1676L-25526, Albuquerque, NM, 2014.

[3] Shenoy, R.R., Drozda, T.G., Norris, A.T., Baurle, R.A., and Drummond, J.P., "Comparison of Mixing Characteristics for Several Fuel Injectors at Mach 8, 12, and 15 Hypervelocity Flow Conditions," in *AIAA Propulsion and Energy Forum*, Cincinnati, OH, 2018.

[4] Adams, B., Eldred, M., Geraci, G., Hooper, R., Jakeman, J., Maupin, K., Monschke, J., Rushdi, A., Stephens, J., Swiler, L., Wildey, T., Bohnhoff, W., Dalbey, K., Ebeida, M., Eddy, J., Hough, P.D., Khalil, M., Hu, K., Ridgway, E., Vigil, D., and Winokur, J., "DAKOTA, A Multilevel Parallel Object-Oriented Framework for Design Optimization, Parameter Estimation, Uncertainty Quantification, and Sensitivity Analysis: Version 6.10 User's Manual," Sandia Technical Report SAND2014-4633, Sandia, 2019.

[5] Schetz, J.A. and Billig, F.S., "Penetration of Gaseous Jets Injected into a Supersonic Stream," *J. Spacecraft. Rockets.*, Vol. 3, No. 11, 1966, pp. 1658–1665.

[6] Mao, M., Riggins, D.W., and McClinton, C.R., "Numerical Simulation of Transverse Fuel Injection," in *Computational Fluid Dynamics Symposium on Aeropropulsion*, NASA-CP-3078, NASA, Cleveland, OH, 1990, pp. 635–667.

[7] Portz, R. and Segal, C., "Penetration of Gaseous Jets in Supersonic Flows," *AIAA J.*, Vol. 44, No. 10, 2006, pp. 2426–2429.

[8] Ogawa, H., "Physical Insight into Fuel-Air Mixing for Upstream-Fuel-Injected Scramjets via Multi-Objective Design Optimization," *J. Propul. Power.*, Vol. 31, No. 6, 2015, pp. 1505–1523.

[9] Ogawa, H. and Boyce, R.R., "Multi-Objective Design Optimization of Fuel Injection for Mixing Enhancement in Scramjets by Using Surrogate-Assisted Evolutionary Algorithms," in *18th AIAA/3AF International Space Planes and Hypersonic Systems and Technologies Conference*, Tours, France, 2012.

[10] VULCAN-CFD, "http://vulcan-cfd.larc.nasa.gov/," 2017.

[11] van Leer, B., "Towards the Ultimate Conservative Difference Scheme. V: A Second-Order Sequel to Godunov's Method," *J. Comput. Phys.*, Vol. 32, No. 1, 1979, pp. 101–136.

[12] Edwards, J.R., "A Low-Diffusion Flux-Splitting Scheme for Navier-Stokes Calculations," *Comput. Fluids.*, Vol. 26, No. 6, 1997, pp. 635–659.

[13] McBride, B.J., Gordon, S., and Reno, M.A., "Thermodynamic Data for Fifty Reference Elements," NASA Technical Paper 3287/REV1, NASA, Cleveland, OH, 2001.

[14] Pulliam, T.H. and Chaussee, D.S., "A Diagonal Form of an Implicit Approximate-Factorization Algorithm," *J. Comput. Phys.*, Vol. 39, No. 2, 1981, pp. 347–363.

[15] Menter, F.R., "Two-Equation Eddy-Viscosity Turbulence Models for Engineering Applications," *AIAA J.*, Vol. 32, No. 8, 1994, pp. 1598–1605.

[16] Conaire, M., Curran, H.J., Simmie, J.M., Pitz, W.J., and Westbrook, C., "A Comprehensive Modeling Study of Hydrogen Oxidation," *Int. J. Chem. Kinet.*, Vol. 36, No. 11, 2004, pp. 603–622.

[17] Wilcox, D.C., *Turbulence Modeling for CFD*, DCW Industries, Inc., La Cañada, CA, 2000.

[18] Baurle, R. and Gaffney, R., "Extraction of One-Dimensional Flow Properties From Multidimensional Data Sets," *J. Propul. Power.*, Vol. 24, No. 4, 2008, pp. 704–714.

[19] Drayna, T., Haag, C., Bartkowicz, M., and Gidzak, V., "LINK3D," Software package, version 1.0.0, GoHypersonic, Inc., 2016.

[20] Drozda, T.G., Drummond, J.P., and Baurle, R.A., "CFD Analysis of Mixing Characteristics of Several Fuel Injectors at Hypervelocity Flow Conditions," in *52nd AIAA/SAE/ASEE Joint Propulsion Conference*, AIAA 2016-4764, AIAA, Salt Lake City, UT, 2016.

[21] Adams, B., Eldred, M., Geraci, G., Hooper, R., Jakeman, J., Maupin, K., Monschke, J., Rushdi, A., Stephens, J., Swiler, L., Wildey, T., Bohnhoff, W., Dalbey, K., Ebeida, M., Eddy, J., Hough, P.D., Khalil, M., Hu, K., Ridgway, E., Vigil, D., and Winokur, J., "DAKOTA, A Multilevel Parallel Object-Oriented Framework for Design Optimization, Parameter Estimation, Uncertainty Quantification, and Sensitivity Analysis: Version 6.10 Theory Manual," Sandia Technical Report SAND2014-4633, Sandia, 2019.